IOP Conf. Series: Materials Science and Engineering **249** (2017) 012013 doi:10.1088/1757-899X/249/1/012013

Measurement of corner separation zone response on a compression ramp to plasma actuation within the hypersonic boundary layer

Brock E Hedlund, Alec W Houpt, Stanislav V Gordeyev and Sergey B Leonov

Institute for Flow Physics and Control, University of Notre Dame, Notre Dame, IN, 46556, USA

bhedlund@nd.edu

Abstract. This study was performed to characterize the dominant frequencies present in the boundary layer uptsream of and in the corner separation zone of a compression surface in Mach 4.5 flow and to determine a control effect of transient plasma actuation on the boundary layer. Schlieren imaging was used to distinguish the corner separation zone for 20°, 25°, and 30° compression ramps mounted on flat plates. Spectra of the natural disturbances present in the boundary layer and separation zone were gathered using a high-speed Shack-Hartmann wavefront sensor and surface mounted PCB™ pressure sensors while varying flow parameters by adjusting total pressure, temperature, and ramp angle. Shallow cavity discharge plasma actuators were used as a high-frequency localized thermal forcing mechanism of the boundary layer. The plasma effect was negligible for forcing frequencies (50 kHz) below the natural dominant frequency (~55-80 kHz). High frequency perturbations that can promote the transition to turbulence were amplified when the plasma forcing frequency (100 kHz) was higher than the natural dominant frequency (~55-80 kHz). This technique can potentially be used for active control of hypersonic boundary layer transition and the supersonic flow structure on the compression surface.

1. Introduction

Scramjet engines provide a reusable and more efficient form of supersonic propulsion for atmospheric flight as compared to rocket engines. An air-breathing supersonic engine (scramjet) is expected to be used to power high-supersonic and hypersonic aircraft aimed at transport missions in the prospective applications. These vehicles are expected to operate at high altitudes, where the air density is low enough to achieve these speeds. This is an advantage for reducing the drag on the vehicle but can cause issues with scramjet operation, one of which is the maintaining of operational stability of the air inlet. Turbulent flow is desired at the inlet of a scramjet so as to reduce flow separation and total pressure loss as the flow interacts with the compression surface and helps prevent inlet unstart [1]. The low air density associated with high altitudes leads to a relatively low Reynolds number that means the transition from a laminar to a turbulent boundary layer does not always occur naturally on the length scales encountered. Since the incoming flow generally has a low magnitude of freestream disturbances, which could promote turbulence, the flow needs to be preconditioned by an aerodynamic surface before being ingested. It has been suggested that the most effective mechanism of tripping the flow is the formation of streamwise vorticity within the boundary layer [2].

There are multiple ways that the flow can be tripped to promote the transition to a turbulent boundary layer. The most employed methods include local barriers, discrete surface roughness, or cross-flow jets.

These mechanical methods can augment the instabilities but have slow response times (orders of magnitude larger than the gasdynamic time scale) and, in general, are only capable of generating a stationary pattern of flow forcing. It can be assumed that unsteady forcing of the boundary layer at the appropriate time scales would be more effective than the steady forcing methods at generating and growing unstable disturbances.It has been shown that thermal methods, such as plasma, can be used to promote the laminar-to-turbulent transition [3]. Plasma based flow control uses electron-molecular interactions that transfer energy from an applied electric field to gas acceleration, heat release and pressure elevation via collisional momentum transfer and plasma-chemical reactions. Plasma actuators provide many advantages to the aforementioned methods; faster response time, no moving parts, a robust installation flush with the surface, adjustable frequency to match flow characteristics and to generate flow disturbances. Being able to adjust the frequency and power deposition of the plasma actuators is a key advantage over the mechanical methods which provide a steady forcing and are optimized for only one flow condition. Plasma flow control has been studied extensively focusing on AC or pulse driven Surface Dielectric Barrier Discharge (SDBD) plasmas [4]. The power deposition and power density are typically too low for SDBD to have much of an effect on high-speed flows. There have also been studies done with plasma flow control in high-speed applications [5].

2. Test Approach

2.1 Experimental Facility Description

Testing took place at the University of Notre Dame in the high enthalpy arc tunnel, ACT-1, in Mach 4.5 flow. Figs. 1 and 2 below illustrate the test section arrangement and pictures of the model within the test facility respectively. The test conditions consisted of: a range of the unit Reynolds number $Re_L \approx 3 - 14 \cdot 10^6\ m^{-1}$ and $T_0 = 300\ K$ (cold flow) stagnation temperature; unit Reynolds number $Re_L \approx 4 \cdot 10^5\ m^{-1}$and $800\ K - 1250\ K$ (hot flow) stagnation temperature; stagnation pressure $P_0 \approx 0.8 - 4\ bar$; flow enthalpy $h \cdot \dot{m} \approx 10\ kW$ (cold flow) and $50\ kW$ (hot flow). "Cold flow" and "hot flow" will be used to distinguish between low-enthalpy and high-enthalpy tests respectively. The experimental model consisted of a flat plate with a sharp leading edge at an angle $\alpha = 15^\circ$. One of three plates were mounted on top of the flat plate to form the compression ramp with a variable angle β. In total, the model measured: length $L = 229\ mm$, width $W = 102\ mm$, and height $H = 19\ mm$. $62\ mm$ upstream of the ramp, a row of electrodes was mounted spanwise through the model. Insulated by a ceramic insert, the electrodes were used to generate a plasma discharge on the top surface of the model. This placement is pointed out in Figs. 1 and 2.

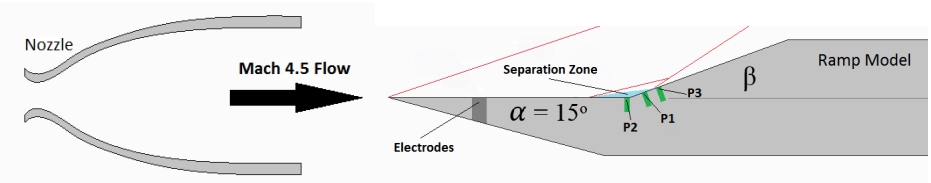

Figure 1. Side view of experimental arrangement.

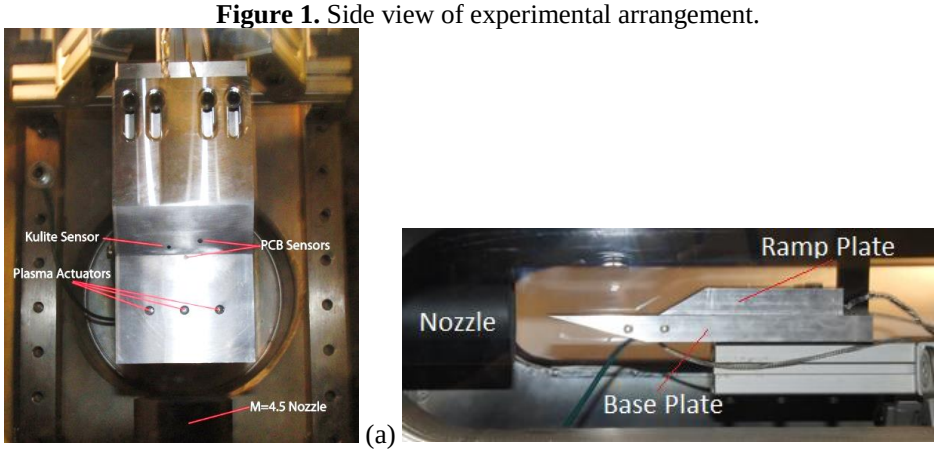

Figure 2. Experimental model in the test section of ACT-1 facility. (a) top view; (b) side view.

Tests lasted up to 1 second, during which the arc heater operated for 0.3 s (for hot flow operation) and plasma generation lasted 0.1 s. The model allows for variations in ramp angles $\beta = 20° - 30°$ in order to vary the corner separation conditions. To establish a baseline and consistency in flow characteristics from one test to the next, data was collected before, during, and after plasma actuation. Instrumentation in the sequence of data collection included a schlieren imaging system, high-speed aero-optical wave front sensor, high speed camera, high sensitivity pressure transducers, and probes to measure current and voltage of the electrical discharge.

Both Kulite™ and PCB™ pressure sensors were selected to provide measurements of the flow pressure and perturbation frequencies within the corner separation zone. A Kulite XCQ-080 miniature pressure transducer provided an absolute pressure measurement within the separation zone at location P1 in Fig. 1. This sensor however, has a limited range of frequency capabilities and measurements are limited to 15 kHz and below, allowing the measuring of the average surface pressure dynamics during the test. A sample of the Kulite sensor measurements is shown in Fig. 3. Pressure amplitude, measured on the ramp at P1 by a Kulite sensor provides pressure profiles for both cold and hot flow tests below.

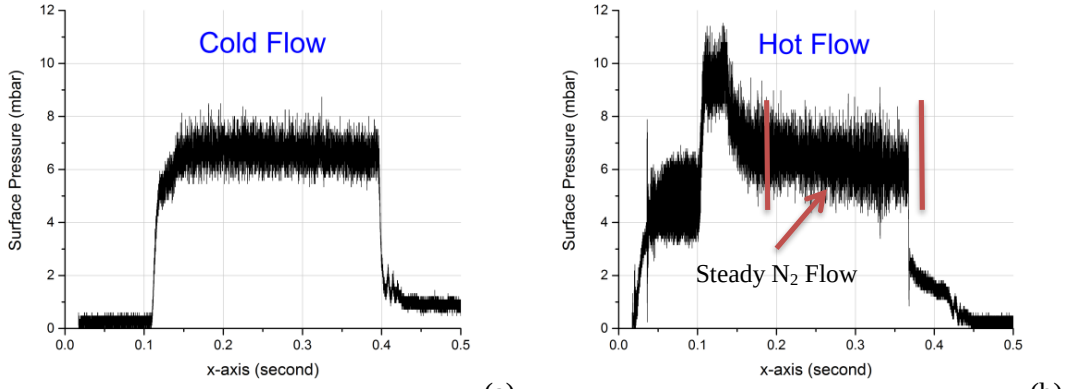

(a) (b)

Figure 3. Pressure data on ramp surface for (a) cold and (b) hot flow tests.

In Fig. 3a, the cold flow profile reflects the steady flow of nitrogen gas for 0.3 seconds. Fig. 3b shows the time sequence for hot flow, beginning with an initial flow of argon gas for approximately 80 ms in order to initiate the arc breakdown. Nitrogen is then introduced prior to the flow of argon cutting out at 0.125 s transitioning the arc to operating in nitrogen only. This data shows the extreme case for the highest pressure to expect in the separation bubble and acts as a guide for the other test conditions.

Two PCB™ 132 series microsensors located at P2 and P3 in Figs. 1 and 2 (only for the $\beta = 30°$ case) provided high frequency pressure measurements in the corner separation zone. The locations of these sensors (on the flat plate and ramp respectively) were chosen to read the traces of perturbation on both surfaces.

Prior to performing the tests with the ramp model, a test was performed to directly measure the freestream speed from the nozzle for both the cold and the hot flow cases using Shack-Hartmann wavefront sensing (principles and setup described later in Section II D). The laser beam was sent normal to the flow direction immediately downstream of the nozzle assembly near the centerline. Deflection angles were gathered with a sampling frequency of 530 kHz on the rectangular grid with 10 points in the streamwise direction and 5 points in the cross direction. A multi-point cross-correlation technique [6] was used to calculate the deflection angle power spectra, phase difference between adjacent streamwise points and the corresponding convective speeds at several points away from the nozzle. It should be emphasized that these are *direct* measurements of the convective speeds of the optically-active small-scale turbulence structures naturally occurring in the freestream.

The extracted deflection angle power spectra at different streamwise points for the cold flow case are presented in Fig. 4. The spectra decay in the streamwise direction, consistent with the isotropic turbulence decaying process. Between frequencies 10 *kHz* and 100 *kHz* all spectra exhibit the power slope of "-4/3", indicated as a dashed line in Fig. 4. In Ref [7] it was shown that this slope corresponds to the Kolmogorov-type spectra of turbulence in the self-similar energy transfer region.

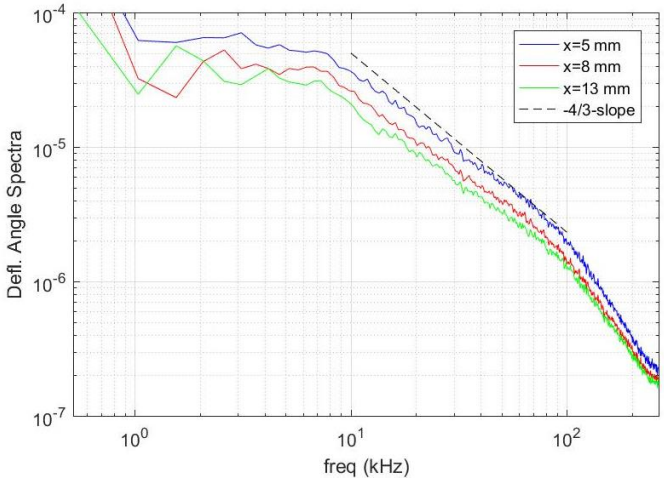

Figure 4. Characterization of the flow disturbances near the nozzle: power spectra

The freestream convective velocities, gathered with the aero-optical technique for the cold flow case at different streamwise points are presented in Fig. 5. The speed is found to be approximately 700 *m/s* immediately after the nozzle. An isentropic calculation of the freestream speed for M = 4.5 and the total temperature of 300 *K*, gives the consistent value of 700 *m/s*. As the flow expands into a vacuum chamber, it forms an under-expanded round jet with a slightly increasing speed further downstream of the nozzle; this effect is also present in Fig. 5. For the hot flow case, the density drops by approximately a factor of 6, compared to the cold flow case, so the optical distortions are reduced by the same factor. Nevertheless, an analysis of the experimental data, performed for the hot flow case, had given the value of the freestream speed between 1,100 and 1,500 *m/s*, with the estimate of the flow stagnation temperature between 800 and 1,250 *K*.

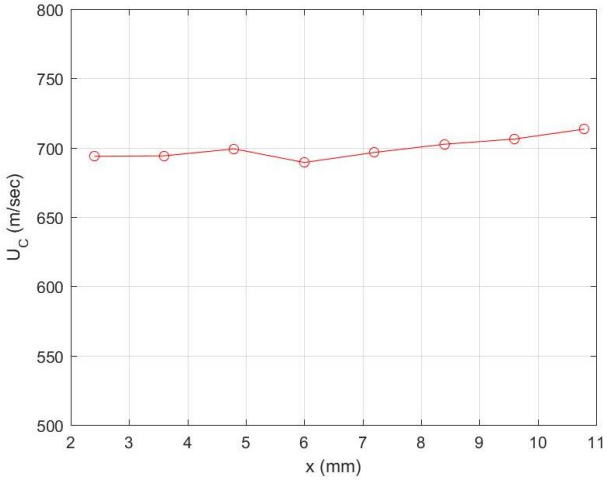

Figure 5. Freestream velocity at streamwise locations for cold flow.

2.2 Estimation of Natural Instability Frequency

The most-amplified naturally occurring disturbances in the test article boundary layer were estimated from Linear Stability Theory results for a flat plate as follows. Fig. 3h in Ref. [8] presents the non-dimensionalized frequency *F* as a function of $(Re_{x,e})^{1/2}$ for an adiabatic flat plate at Mach 4.5. The non-dimensional frequency *F* is defined as:

$$F \equiv \frac{2\pi f}{U_e Re_e} \tag{1}$$

where *f* is the disturbance frequency, U_e is the boundary-layer edge velocity, and Re_e is the unit Reynolds number at the boundary-layer edge.

For a flat plate at zero angle of attack, the unit Reynolds number at the boundary-layer edge equals the freestream unit Re; for these test conditions ($P_0 = 0.8\ bar, T_0 = 300\ K$), $Re_e = 3.0 \cdot 10^6\ /m$. The Reynolds number based on the distance from the leading edge to the ramp ($x = 0.10\ m$) and boundary-

layer edge conditions, $Re_{x,e}$, for this test condition is thus $3.0 \cdot 10^5$. According to Fig. 3h in Ref. [8], for $(Re_{x,e})^{1/2} = 539$, $F \approx 7.8 \cdot 10^{-5}$ then the dominant frequency to be expected is $f \approx 25\ kHz$. The low-enthalpy case has an approximately adiabatic wall. In the high-enthalpy case, the wind tunnel run time was too short to reach an adiabatic wall, so the relatively cold wall would result in a thinner boundary layer and somewhat higher disturbance frequency [9].

It should be noted that this approximation is extrapolated from Fig. 3h in Ref. [8], so it is not 100% reliable. It also must be noted that the Reynolds number used in the experiments are significantly lower than the studies done, so the disturbances may not yet have enough time to develop and grow to become well-observable.

When the total pressure is increased to $2.2\ Bar$, the unit Reynolds number increases to a more reasonable value of $Re_e = 8.0 \cdot 10^6\ /m$. This increases the predicted most amplified frequency of perturbations to be $f \approx 55\ kHz$. Neutral stability curves for this case are presented in Fig. 10.5 of Ref. [9]. The point corresponding to $(Re_{x,e})^{1/2} = 894$ and $F \approx 6.3 \cdot 10^{-5}$ is well within the unstable region for first-mode (Tollmien-Schlichting) waves. The maximum stagnation pressure tested was $4\ Bar$ which corresponds to a unit Reynolds number of $Re_e = 14 \cdot 10^6/m$, $(Re_{x,e})^{1/2} = 1200$, and $F \approx 4.7 \cdot 10^{-5}$. This is again well within the first-mode unstable region. The most amplified frequency for this max case is $f \approx 78\ kHz$.

Due to the extremely low Reynolds number while testing with stagnation pressures under $1\ Bar$ and the linear stability prediction, the perturbations seen in these cases are not believed to be first mode (Tollmien-Schlichting) waves. Alternatively, it follows that these could be second mode acoustic vibrations in nature. Assume the measured separation zone thickness of $\delta = 1.8\ mm$ is one-quarter of the wavelength of some acoustic wave ($\lambda = 7.2\ mm$). Assuming the temperature of the boundary layer is approximately equal to the total temperature, $T_0 = 300$, the local sonic velocity is $a = 353\ m/s$. Using the equation $f = a/\lambda$ the estimated frequency of this acoustic wave is $49\ kHz$. Using the same method for hot flow, the estimated frequency is $127\ kHz$.

2.3 Approach to the Plasma Actuator Design

The fast development of a gas dynamic instability can be promoted by the introduction to the system of an oscillation of pressure or gas density, with a proper frequency, to the boundary layer. The main method for doing so is a modulation of the electrical power deposited to the plasma. This method might not be fast enough because the response time is limited by the gas dynamic time scale, related to a characteristic length of a few centimeters. At the same time, a modulation of electrical parameters of the plasma might initiate much faster kinetic processes in the gas flow.

Over the last few years, kinetic mechanisms of "rapid heating" resulting from energy transfer from internal molecular energy to translational/rotational temperature, on a sub-microsecond time scale, have been analyzed in great detail [10]. This suggests that rapid heating, caused primarily by the quenching of N_2 excited electronic states by oxygen, $N_2^* + O_2 \rightarrow N_2 + O_2$, would result in significant pressure overshoot in the plasma zone [11]. The process of gas dissociation may deliver even faster pressure elevation, although with a lower overall efficiency. In a multicomponent gas (air), the gas pressure can be represented by the sum of partial pressures of each component. The equation takes into account the ionization with degree α and the dissociation of a molecular gas with degrees δ_k for the k-component (N2, O2, at least). For the dissociation of multiatomic molecular gases the dissociation degree is defined as $\delta_k = \frac{\sum_i N_{ki} - N_k}{N_k}$, where i-species are originated due to k-species dissociation. Thus the gas pressure is

$$P = k_B \cdot \sum_{k=1}^{m} N_k \cdot T_k \approx\approx k_B \cdot (N_{N2} + N_{O2}) \cdot \left((1 + (1-\chi) \cdot \delta_{N2} + \chi \cdot \delta_{O2}) \cdot T_g + \alpha \cdot T_e\right) \quad (2)$$

Here k_B is the Boltzmann constant and χ the molar fraction of molecular oxygen in the gas. Nitrogen dissociation is negligibly small at these conditions. If only fast processes are considered (frequency $f \geq 10^5\ Hz$), for the rough estimation the gas density can be posed as a lesser variable than the gas temperature and pressure. After simplification the pressure dynamics can be expressed by the following formula:

$$\frac{dP}{dt} \approx k_B \cdot (N_{N2} + N_{O2}) \cdot \left((1 + \chi \cdot \delta_{O2}) \cdot \frac{\partial T_g}{\partial t} + \chi \cdot \frac{\partial \delta_{O2}}{\partial t} \cdot T_g\right) \quad (3)$$

Note, that the derivative of the dissociation degree can be calculated through a dissociation reaction rate coefficient k^d_{ki} (2nd order). :

$$\frac{\partial \delta_k}{\partial t} = \frac{1}{N_k} \cdot \sum_i \frac{\partial N_{ki}}{\partial t} = \sum_i (k^d_{ki} \cdot N_k - k^r_{ij} \cdot \frac{N_{ki} \cdot N_{kj}}{N_k}) \quad (4)$$

where the recombination processes with rate coefficients k^r_{ij} could be neglected with fast temperature elevation.

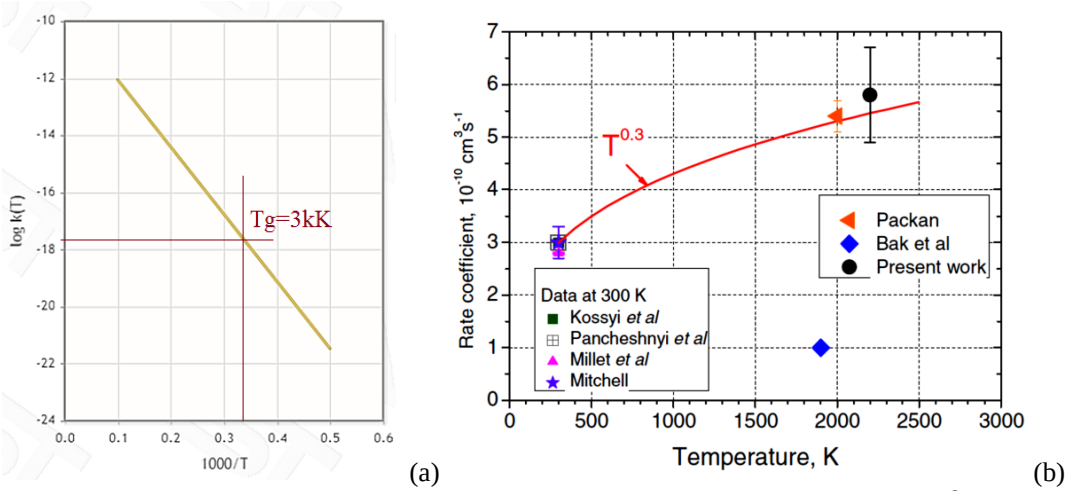

(a) (b)

Figure 6. Thermal dissociation rate constant. (a) reaction O2 (thermal) = O + O [k]=m^3/s [12]; (b) reaction N2*+O2=N2+O+O - quenching rates of N2(C) by O2 [13].

The measurements performed in a nanosecond duration discharge [13] confirm that the ultrafast dissociation of molecular oxygen is mainly due to the quenching reaction of N2(B) and of N2(C) by oxygen. The fraction of dissociated oxygen reaches about 50% after 20 ns. Both the gas temperature evolution and oxygen density are in good agreement with the ultrafast mechanism simulations of Popov [10, 14]. The fraction of energy spent on dissociation of oxygen is about 35%, and the fraction of energy spent on gas heating is about 21%. Figure 6 presents data on reaction rate constants for thermal dissociation of oxygen and oxygen dissociation in low-temperature pulsed plasma. It is well seen that a thermal dissociation of oxygen does not play a significant role in pressure elevation even at gas temperature $T_g \approx 3kK$, compared to the non-equilibrium dissociation in plasma. The effect of the plasma-based dissociation might be >10^3 times higher than one due to the thermal mechanism. To realize such a mechanism, the plasma should be organized in a proper way. It is also important that in the case of a plasma kinetic mechanism the upper boundary of the frequency of pressure oscillations is not limited by a slow, purely thermal, process.

Existing data [15] allows suggestion that the most effective frequency of artificial disturbances for tripping the boundary layer for excitation of the first mode of BL disturbances at $M = 5$ is $f = 100 - 200\ kHz$. For a proper optimization of the system, the frequency of plasma operation has to be adjustable over a wide range. Previously, data was collected with isolated roughness elements installed in one line in the spanwise direction with 5 to 25 mm spacing [2]. Based on suggestion to produce the local instant gas temperature increase $\Delta T \approx 10^2 - 10^3\ K$ the average electrical power of each actuator should be in the range of $P = 100 - 500\ W$. The duration of each plasma pulse should be of microsecond or submicrosecond scale to produce pointwise disturbances. A low level of gas density in a hypersonic boundary layer flow may cause an issue because in a low gas density environment the discharge strives to transit to a glow type discharge where the power density becomes too low for any observable effect. Preliminary tests [16] indicate that it is possible to generate filamentary plasma at the molecular concentration of $n > 2{\times}10^{17}\ cm^3$ using a simple two-electrode scheme.

The Shallow Cavity Discharge actuator [16] has been used in these tests. It is flush mounted, with a size of a few millimeters, and can be installed on the metallic surface of the model. It has the proper discharge geometry, reasonably low applied voltage, and a sufficient level of the disturbances excited. A time resolved image of the SCD discharge in $M = 4.5$ flow taken by the Andor iStar ICCD camera is shown in Fig. 7. At $f = 50 - 100\ kHz$, the discharge works as a push-pull plasma mini-jet. At lower

frequencies of repetition a second operation mode was observed, currently considered as a cathode sheath pattern, where a rather thin layer of plasma covers most of the model surface. The cathode sheath is where a major portion of the electric power is released [17] that is potentially beneficial for BL control.

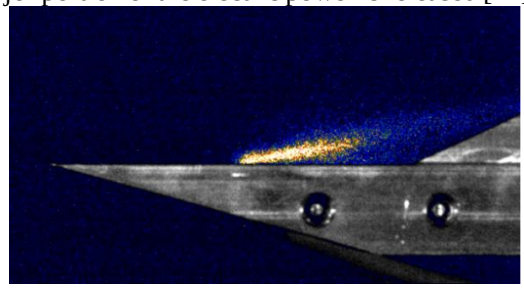

Figure 7. SCD in $M = 4.5$, $P = 4\,mbar$ flow in plasma mini-jet operation mode. Exposure 1μs, delay time 3 μs (within the electric pulse).

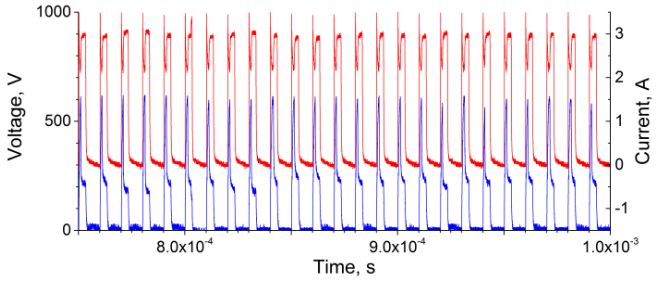

(a)

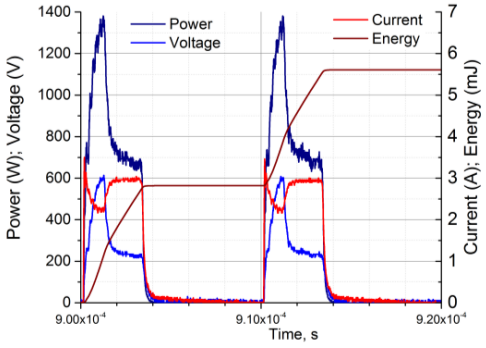

(b)

Figure 8. Voltage –current time series of the SCD operation at $f = 100\,kHz$ (a); calculation of the discharge pulse power and energy for 3 SCDs (b).

Typical records of the electric parameters in M=4.5 flow are shown in Fig. 8a for a frequency of repetition $f = 100\,kHz$. The pulse energy and average power were calculated based on this data, as it is shown in Fig. 8b. The discharge parameters were as follows: frequency of repetition $f = 10 - 100\,kHz$; pulse duration $t < 4\,\mu s$; voltage $U < 1\,kV$; pulse energy $E = 0.8 - 1.2\,mJ\,/unit$; average power $W_{av} < 400\,W$. Three units of SCD have been arranged in the model.

2.4 Aero-Optical Measurements

Aero-optical diagnostic measurements were performed using a high-speed Shack-Hartmann wavefront sensor [18]; a schematic of the experimental setup is shown in Fig. 9. The laser beam was expanded to a 50-mm-diameter collimated beam and passed along the spanwise direction over the corner region of the model mounted in the test section. The spanwise beam propagation was chosen for two reasons. First, the flow is expected to be primarily spanwise-uniform. Second, as the beam traverses the 4-inch-long region of the flow, aero-optical distortions become stronger thus improving the signal-to-noise ratio [19]. After exiting the test section, the beam is reflected off the return mirror, which sends the beam back along the same path. This so-called double-path setup further amplifies the aero-optical signal by a factor of two, as the beam traverses through the flow of interest twice, and also simplifies the optical setup. The returning beam is split off using a cube beam splitter, sent though a contracting telescope, which reduces the beam size to 12.5 mm in diameter, and recorded by a Phantom v1611 high-speed digital camera. The camera had a 38 mm focal length, 70×60 lenslet array with 0.3-mm-pitch with 100% fill ratio, attached to it. After passing through the lenslet array, the beam was split into subaperture beams

and focused on the camera sensor, creating a series of dots. To achieve the high, 531 kHz, sampling rate, only a small portion of the image (128×64-pixel) was acquired for the full duration of the tunnel run. In-house software was used to extract the temporal motion of the dots and to convert this into a time series of the deflection angles.

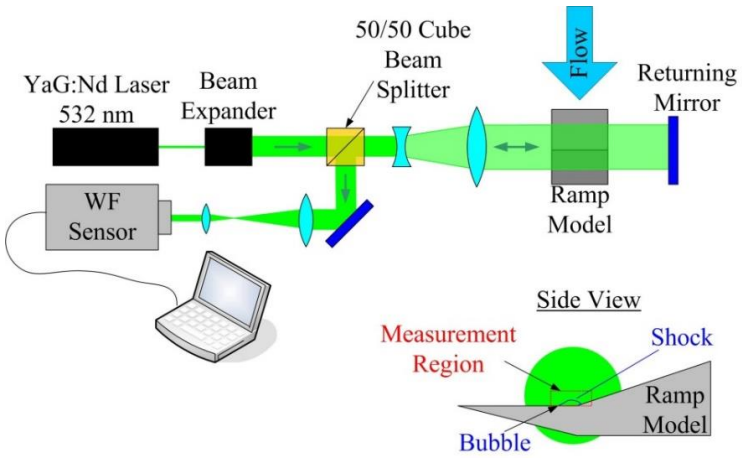

Figure 9. Schematic of set-up for aero-optical measurements.

It is important to note that all aero-optical measurements are non-intrusive by nature, sensitive to the density field only, provide good spatial resolution and limited in temporal resolution only by the digital camera technology. Comparing to other optical diagnostics, like schlieren or shadowgraph techniques, wavefront measurements provide additional advantages. The light from each lenslet is focused on a digital sensor, increasing the dot intensity, so wavefront measurements can be done with less-powerful lasers. A location of the dot is typically extracted with better than 0.1 pixel resolution using centroiding algorithms [20], providing accurate measurements of the deflection angle over the subaperture, since the displacement of each dot is proportional to the subaperture-averaged deflection angle. The time series of the deflection angles carry information about the temporal characteristics of the density field over different spatial locations across the laser beam. The wavefront sensor simultaneously measures both streamwise (X-) and wall-normal (Y-) components of the deflection angle; this is in contrast to Schlieren, where wavefront changes are measured along only one fixed direction. The 2-component deflection angle is a local gradient of the wavefront, so knowing both components of the deflection angle the wavefront (or equivalently, Optical Path Difference or OPD) can be computed. OPD is proportional to the spanwise-integrated density field, $OPD(x,y,t) = K_{GD} \int \rho'(x,y,z,t)dz$ [21], where K_{GD} is the Gladstone-Dale constant, and knowing OPD, the amplitude of the density fluctuation over a subaperture can be estimated [19]. In contrast, time-resolved Schlieren images provide good spatial and temporal information, but density information is not easily extracted from them. Finally, the wavefront measurements using the Shack-Hartmann sensor are fairly insensitive to mechanical vibrations, imposed on the test section, the model and different components of the set-up [21].

3. Test Results

For all tests it was important to distinguish the formation, stability, and size of the corner separation zone. Schlieren images were made using a pulsed NIR laser diode with a pulse duration of $0.15\ \mu s$, essentially showing the flow for one moment in time to examine these separation zone characteristics in $M = 4.5$ flow. It was observed that the corner separation zone forms and stabilizes within $15\ ms$ of the flow starting. Fig. 10a notes the important features of the flow field on a schlieren image. The low Reynolds number of the flow in these experiments causes the laminar boundary layer, resulting in the flow separation for all three ramp angle cases, as it is seen in the $25°$ and $30°$ in Figs. 10c and 10d. There is a shallow separation zone, much longer than it is deep, for the $20°$ case in Fig. 10b. This shallow separation zone with laminar boundary layers was also found numerically in Ref. [22].

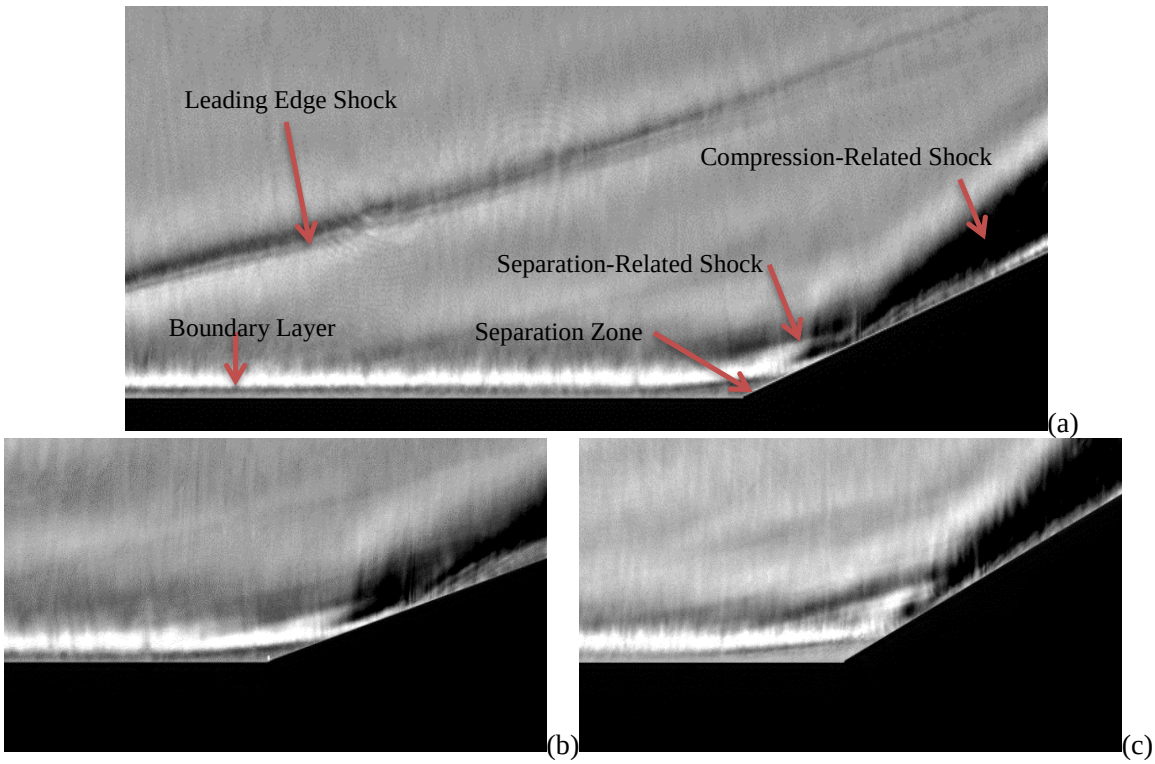

Figure 10. Schlieren images of the ramp corner and the full flow field with ramp angle: (a) 25° and enlarged separation zones for: (b) 20° and (c) 30°.

To gather basic information about the flow field, both a Shack-Hartmann wave front sensor and surface mounted PCB™ sensors were used to collect data on the perturbations in the flow. The aero-optical method measures the gas density gradients at multiple points in the flow field while gathering data at the surface with pressure sensors can provide more information about the boundary layer conditions. The ramp angle and total pressure, P_0, were varied to observe the effects of each on the amplitudes of flow perturbations present. The two PCB™ sensors, mounted at P2 and P3 (see Fig. 1) detected flow perturbations on the flat plate and ramp portions of the model surface. The data collected on the flat plate with varying total pressure and ramp angle is shown in Fig. 11 and the ramp data collected for the 30° case is shown in Fig. 12.

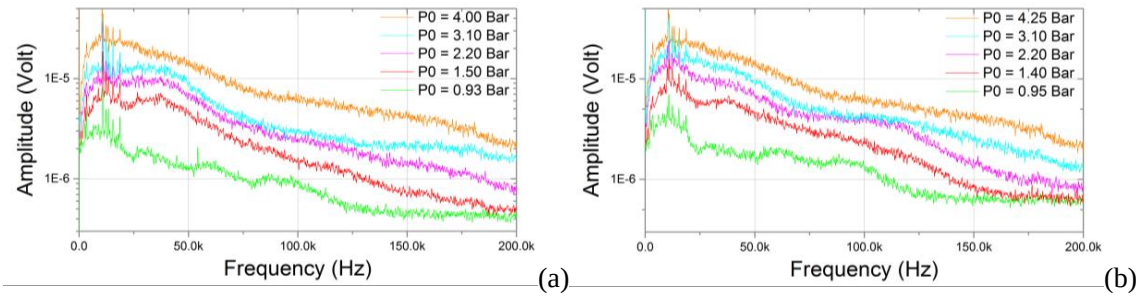

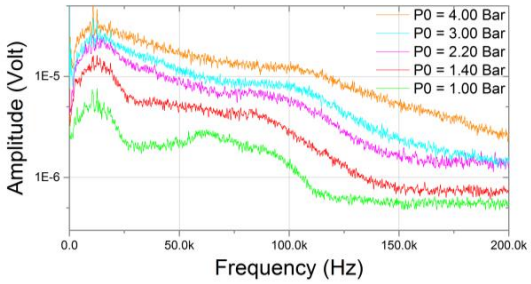

(c)

Figure 11. Spectra of flow disturbances measured on the flat plate by a PCB™ pressure sensor with ramp angle: (a) 20°, (b) 25°, and (c) 30°.

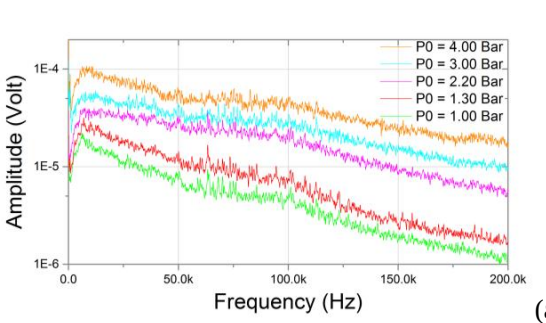

(a)

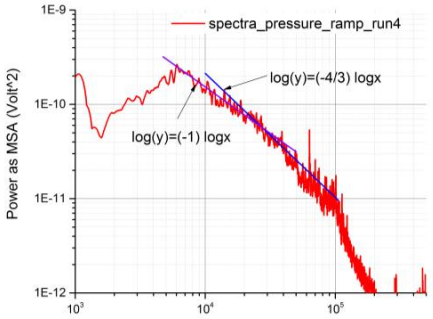

(b)

Figure 12. (a) Spectra of flow disturbances measured on the ramp surface near the separation zone on a 30° ramp and (b) log-log plot of pressure spectra

It can be seen that the total pressure has a significant effect on the spectra of the pressure perturbations. The increase in total pressure results in a higher unit Reynolds number flow with a significantly higher magnitude of initial perturbations in the flow; this is seen as a higher magnitude of oscillations across the frequency spectrum. A higher total pressure also shifts the peak of the dominant frequencies higher. In Fig. 11c the dominant peak for $P_0 = 1\ bar$ is approximately $F = 60\ kHz$. The peak broadens and shifts to the right such that for $P_0 = 2.2\ bar$ the peak is $F > 75\ kHz$. This shifting effect can also be attributed to a change in the unit Reynolds number, which has a significant impact on the development of the boundary layer and the perturbations present. The dominant peak structure tends to become less dominant and all frequencies experience an increase in amplitude as the stagnation pressure increases to $P_0 = 4\ bar$. The same effect of increasing magnitude is observed in the data collected on the ramp surface in Fig. 12a, where the spectra are nearly an order of magnitude higher. Fig. 12b is a sample of ramp data plotted on a log-log scale. Here, the "-1" power slope in the mid-range frequencies is associated with eddy motion in the logarithmic layer of the boundary layer [23]. The "-4/3" power slope of the higher frequencies suggests that the flow is turbulent. Flow tends to transition to turbulence quickly after the reattachment point with corner separation zones.

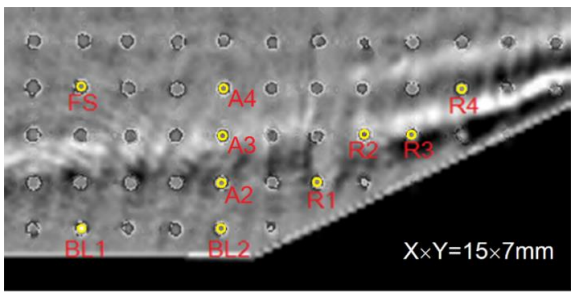

(a)

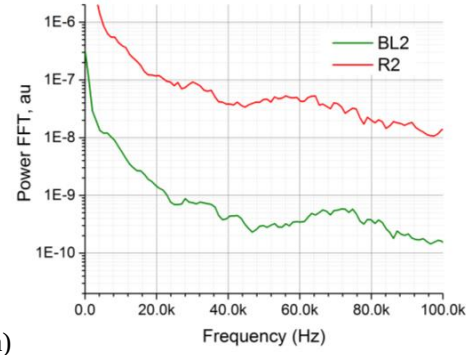

(b)

Figure 13. (a) shawdowgraph and measurement locations; and (b) FFT spectra of optical density perturbations.

To better visualize the relation between the spatial distribution of the deflection angles, measured by the wavefront sensor, and the flow structure in the vicinity of the flow separation zone, the same optical setup was used to obtain high-speed shadowgraph videos. The lenslet array was removed and distorted intensity patterns were recorded at the same sampling speed of 531 kHz over the same 64×128 area. This image size corresponds to a 15×7 mm measurement region over the model. The representative shadowgraph image with an overlaid dot pattern (with 1.2 mm spacing between the dots) from time-averaged Shack-Hartmann wavefront sensor images is shown in Fig. 13a. The flow regions, indicated by yellow circles in Fig. 13a, were selected to investigate the temporal dynamics and the flow structure sensitivity to the plasma generation, specifically: point BL2 is inside the separation zone, A2 and A3 correspond to the unsteady shock over the separation zone, and A4 is in the outside portion of the flow downstream of the plasma generators.

Figure 13b demonstrates the optical density fluctuation spectra taken by the aero-optical technique to be compared to the pressure sensor dataset. Two lines of observation have been chosen to be close to the locations of the pressure sensors. The major frequency of disturbances, measured by the two techniques is similar, thus initially verifying both techniques and proving that the perturbations are indeed flow related and not due to some sensor characteristic. The aero-optical technique was used to determine the perturbation frequencies present in the boundary layer upstream of the corner separation zone. Fig. 14 below shows this data for cold and hot flows on a 30° ramp and Fig. 15 shows the corresponding measurement locations in this test series. Figure 14a indicates that as the boundary layer approaches and enters the corner separation zone that the peak frequency shifts lower. This effect is less apparent in Fig. 14b. It is difficult to optically determine the oscillations of the boundary layer prior to the separation zone due to the extremely low density of the gas. Here the appearance of the local maximum at $F \sim 110\ kHz$ at BL8 and BL9 correspond to the measurement points being in the corner separation zone.

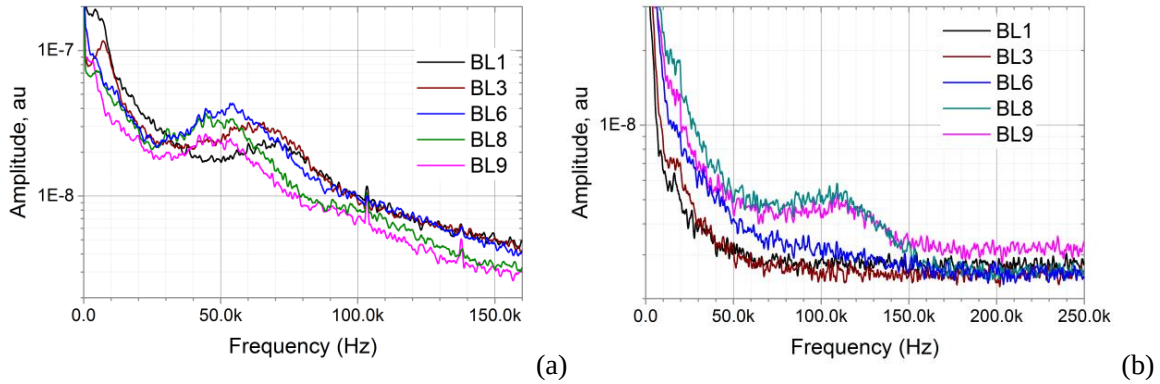

Figure 14. Wavefront oscillation spectra for different positions along the plate: (a) cold flow; (b) arc-heated tests.

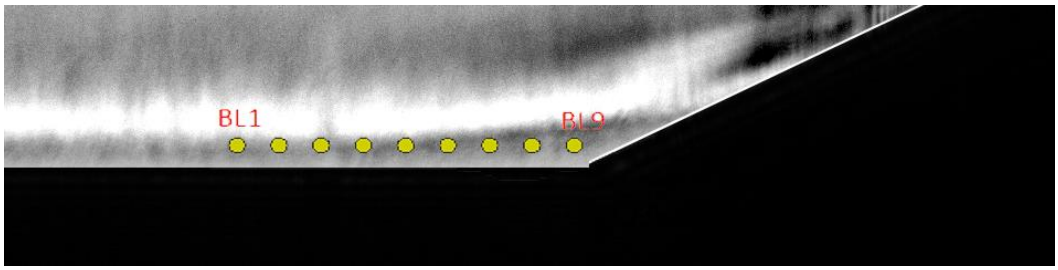

Figure 15. Shack-Hartmann data points overlaid on a schlieren image used for measurements of the BL condition.

Figure 16 compares the data collected with the Shack-Hartmann to pressure sensor data for a 30° ramp. The pressure sensor data was normalized to equalize the magnitude of the signal in the two methods. The datasets appear to agree quite well. Some shift in the peak frequency for Figs. 16a and 16b as well as an increase in amplitude for Fig. 16b is observable which can be attributed to a few

factors. The pressure sensor is measuring pressure oscillations whereas the Shack-Hartmann measures density oscillations. These two properties are indeed related but not necessarily the same. Also, there is a difference in sensitivity to what is being measured. The pressure sensors are more sensitive than the optical measurements, hence why the data had to be normalized after transforming to the frequency domain. This factor can account for the larger amplitude of the peak frequency in Fig. 16b.

None of the results follow the linear stability theory predictions. Recall that the peak frequencies seen in Fig. 16 are not believed to be T-S waves, but instead are trapped acoustic disturbances. The estimated 49 kHz and 127 kHz match well with the data in Fig. 16 thus improving the validity of the origin of the perturbations. The peak dominant frequency differs between the cold and hot flow cases. It is expected for the dominant frequency to be higher in the hot flow case since the sonic velocity and flow speed are higher, affecting the acoustic resonance frequency. In addition, the run time is so short that the model walls do not have time to reach adiabatic conditions resulting in a cooling effect on the boundary layer. This can also cause the boundary layer to be thinner, resulting in an extra shift to a higher dominant frequency.

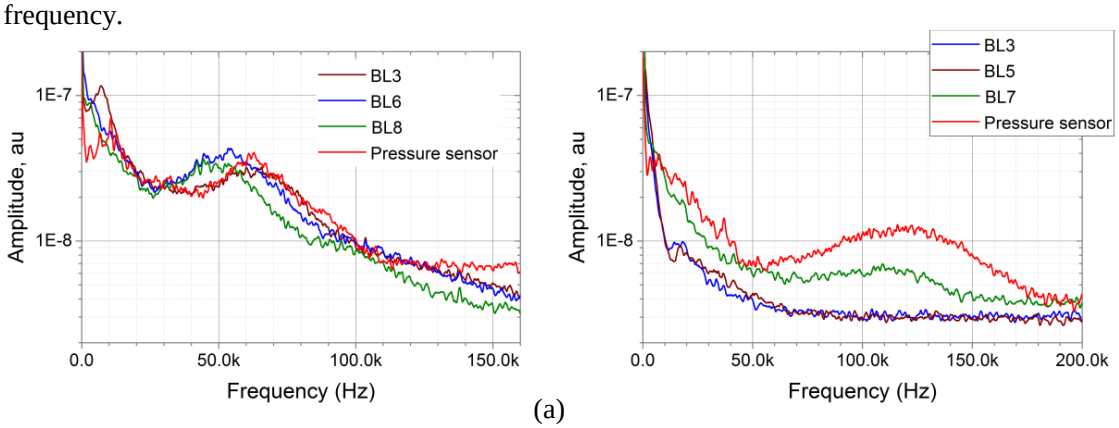

Figure 16. Spectral data comparison including Shack-Hartmann wavefront sensor and pressure sensor: (a) low enthalpy test; and (b) high enthalpy test.

With the dominant natural frequencies present in the boundary layer determined under these test conditions it was then possible to study the effect of pulse-repetitive SCD operation on the spectra of flow perturbations in and near the corner separation zone. Deflection-angle spectra obtained using the high-speed Shack-Hartmann wavefront sensor were analyzed at the locations indicated in Fig. 13a. Note, the use of the pressure sensors is challenging under these conditions due to a high level of the electromagnetic noise associated with the plasma operation. Early results showed [24] that SCD operation affects the spectra only slightly if the repetition frequency is less than the dominant frequency of the first-mode instability, $F_1 = 60 - 80\ kHz$. Operating at a frequency greater than F_1 produces significant changes in the spectra of disturbances.

As mentioned above, the wavefront sensor measures horizontal (X) and vertical (Y) components of the wavefront gradient. Isotropic flows generally display close to equal magnitudes of the wavefront gradient in the horizontal and vertical directions. The near-wall flow considered in this study is expected to have larger magnitudes of deflection angles in the wall-normal (Y) direction compared to the streamwise (X) direction as a result of the larger density gradients in the wall-normal direction. This in turn amplifies the effect that the plasma has on exciting the higher frequency disturbances and results in larger magnitudes of deflection angles.

Figures 17a-d show data for plasma actuation at a frequency of 100 kHz for two points in the incoming boundary layer and two points near the compression ramp (refer to Fig. 13a for the corresponding measurement points). Each test included measurements of 0.1 s prior to plasma actuation, and 0.1 s during plasma operation. There appears to be a small effect due to the plasma in the boundary layer at point BL1 (see Fig. 13a). At the point BL2, Fig. 17b, the amplitude of perturbations is higher and the amplitude of high-frequency disturbances larger than $F = 80\ kHz$ increases. However, looking at Figs. 17c and 17d gathered for the ramp locations, it can be seen that these high-frequency disturbances were excited at the cost of a significant reduction of the peak frequency oscillations.

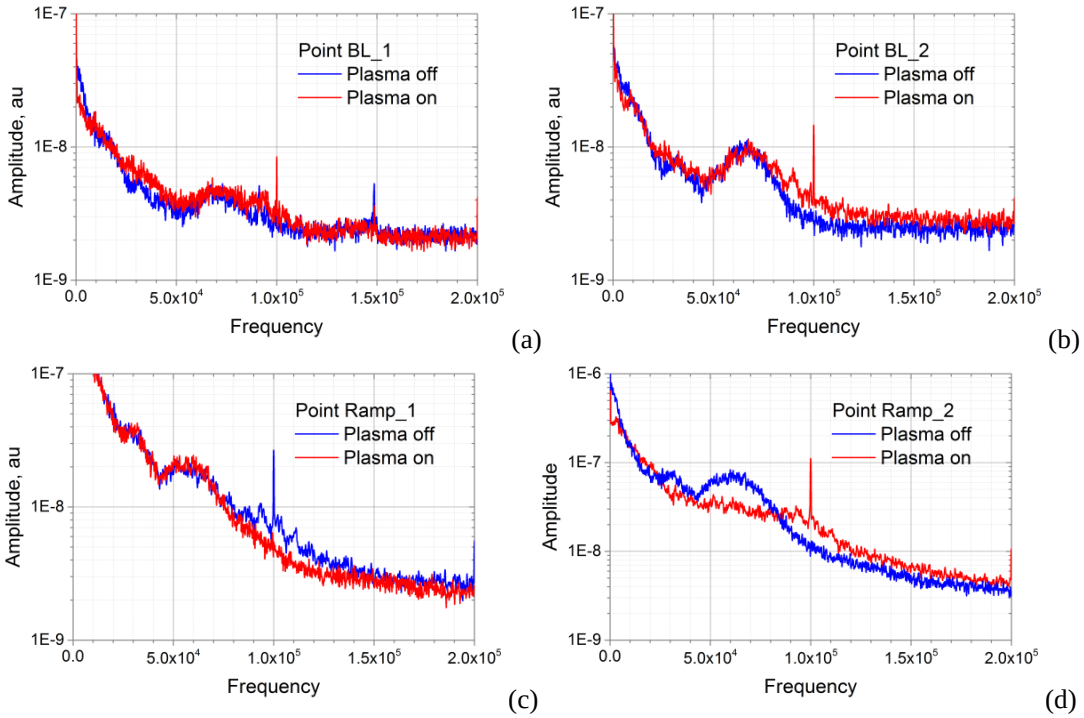

Figure 17. Spectra of flow disturbances. Y-component of the deflection-angle spectra, plasma excitation $f = 100\ kHz$. (Fig. 13a for reference)

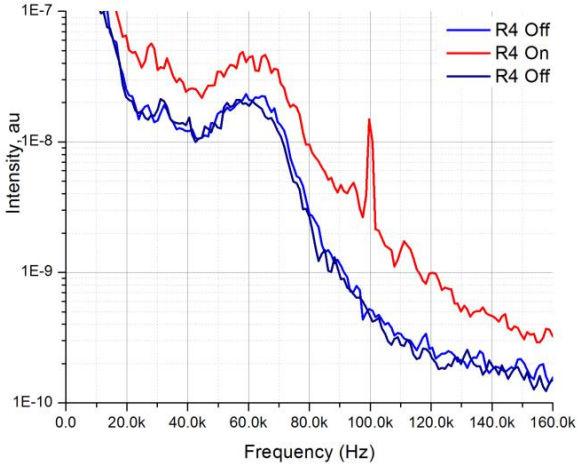

Figure 18. Spectra of flow disturbances on the ramp, point R4 (Fig. 13a for reference).

Figure 18 displays the spectra of flow perturbations at the point Ramp_4 with the largest observed plasma effect. Here the data is presented for three time periods: before the SCD plasma actuation, during SCD actuation, and after the SCDs are turned off. This was done to ensure that flow parameters did not change during operation. Point R4 lies on the compression ramp and is very near the reattachment point of the boundary layer to the ramp. The magnitude of the flow disturbances was increased for all observed frequencies and even extends beyond $100\ kHz$. The resulting amplification of flow perturbations at R4 due to the operation of the SCD actuators is $A/A_0 = 2 - 8$. It may reflect the earlier transition of the flow to a turbulent state on the compression ramp after the separation reattachment.

4. Conclusion

A canonic geometrical configuration has been tested in $M = 4.5$ high-enthalpy flow consisting of a flat surface at zero angle of attack and a compression ramp with inclinations of 20, 25 and 30 degrees in order to vary the size of the corner separation zone from a negligibly small one to a well-detected area

characterized by the appearance of an oblique shock wave originating from a wedge of the separation zone. The spectra of gas pressure perturbations were gathered from surface mounted pressure sensors and compared to the gas density perturbations measured non-intrusively by a high-frequency Shack-Hartmann sensor (aero-optical technique). The dominant frequency in the boundary layer was detected in the range of $F = 55 - 70\ kHz$ in cold flow ($T_0 = 300K$) and $F = 90 - 120kHz$ in hot flow ($T_0 = 800 - 1250K$). There is a shift to lower frequencies as the boundary layer approaches the corner separation zone. It is believed that this is due to the increasing thickness of the boundary layer, especially once it reaches the corner separation zone. This increase in boundary layer thickness increases the wavelength of the trapped acoustic waves, thus decreasing the frequency. Varying the ramp angle had little effect on the dominant frequencies present.

Employing pressure sensors with high-frequency capabilities allowed for the verification of the results obtained from the aero-optical techniques and vice-versa. The Shack-Hartmann sensor collected data about the flow field density perturbations, while the pressure sensors collected pressure oscillation data at the surface. The aero-optical techniques employed have high potential for use in high-speed flows due to the ability to gather data in a non-intrusive way at high-frequencies (as high as $1\ MHz$), with a high spatial resolution, in the range of $1 - 2\ mm$. Utilizing optical methods and surface mounted pressure sensors it is possible to determine the flow perturbations in the flow field, on the surface and their cross-correlation.

An attempt to control the flow field pattern in the compression configuration of the flow has been performed with application of a highly-transient plasma generator arranged midway between the test model leading edge and the compression ramp. The generation of a constricted plasma in a low-density gas, characteristic of high-speed boundary layers, is of utmost importance in actually being able to affect the flow structures on the appropriate time scales. The shallow cavity discharge has been shown to fit this need and is still being studied to define the full limits of its operation. The hope is to be able to push its operating frequency to $f > 200\ kHz$ and beyond while maintaining its power density such that it can be utilized in a wide range of high-speed flows into the hypersonic range. The specific geometry of the SCDs used, a one-dimensional array of plasma elements in the spanwise direction with individual control of each element, has demonstrated its effectiveness in exciting high-frequency disturbances within the boundary layer. These tests have also demonstrated the feasibility of high repetition rate plasma operation in low-density, high-speed flow. Looking at all of the data collected, it is reasonable to conclude that hypersonic boundary layers are sensitive to highly transient plasmas. Active tripping of the boundary layer by electrical discharges can be done for a wide range of flow conditions so long as the forcing frequency is higher than the dominant frequency of perturbations present in the boundary layer; $f > F$.

Going forward, it is proposed to gather more data for varying flow conditions, most importantly an increased Reynolds number. Linear stability theory predicted for a flow case with $P_0 = 2.2\ bar$, the dominant first mode frequency would be $55\ kHz$ and is well within the unstable region for first mode waves as should be when $P_0 = 4\ bar$. It is also considered to study the geometry of the model and how the location of the plasma actuators in relation to the leading edge can affect the receptivity to perturbations that will grow nonlinearly. If the ramp location is moved further away from the leading edge, it is possible to have second mode waves of acoustic nature play a role in transitioning to turbulence which could also be utilized.

5. References

[1] Valdivia A, Yuceil K B, Wagner J L, Clemens N T and Dolling D S 2014 Control of Supersonic Inlet-Isolator Unstart Using Active and Passive Vortex Generators *AIAA Journal* **52** 6 pp 1207-1218

Wu Y, Yi S, He L, Chen Z and Zhu Y 2015 Flow Visualization of Mach 3 Compression Ramp with Different Upstream Boundary Layers *Journal of Visualization* **18** pp 631-644

[2] Berry S A, Nowak R J and Horvath, T J 2004 Boundary Layer Control for Hypersonic Airbreathing Vehicles *34th AIAA Fluid Dynamics Conference* AIAA-2004-2246 Portland Oregon

Schneider S, "Effects of Roughness on Hypersonic Boundary-Layer Transition," *Journal of Spacecraft and Rockets,* **45**, no. 2, pp. 193-209, 2008.

Reshotko E and Tumin A, "Role of Transient Growth in Roughness-Induced Transition," *AIAA Journal,* **42**, no. 4, pp. 766-770, April 2004.

Choudhari M, Li F and Edwards J, "Stability Analysis of Roughness Array Wake in a High-Speed Boundary Layer," in *47th AIAA Aerospace Sciences Meeting, AIAA-2009-170*, Orlando, Florida, 5-8 January, 2009.

[3] Yan H and Gaitonde D, "Effect of Thermally Induced Perturbation in Supersonic Boundary Layers," *Physics of Fluids,* **22**, no. 064101, pp. 1-17, 2010.

[4] Adamovich I V, Little J, Nishihara M, Takashima K and Samimy M, "Nanosecond Pulse Surface Discharges for High-Speed Flow Control," in *6th AIAA Flow Control Conference, AIAA 2012-3137*, New Orleans, Louisiana, 25-28 June, 2012.

Corke T, Enloe C and Wilkinson S, "Dielectric Barrier Discharge Plasma Actuators for Flow Control,," *Annual Review of Fluid Mechanics,* **42**, pp. 505-529, 2010.

Kotsonis M, Correale G, Michelis T, Ragni D and Scarano F, “Nanosecond-Pulsed Plasma Actuation in Quiescent Air and Laminar Boundary Layer," *Journal of Physics D: Applied Physics,* **47**, no. 10, p. 105201, 2014.

Kriegseis J, Duchmann A, Tropea C and Grundmann S, "On the Classification of Dielectric Barrier Discharge Plasma Actuators: A Comprehensive Performance Evaluation Study," *Journal of Applied Physics,,* **114**, no. 053301, 2013.

Leonov S, Opaits D, Miles R and Soloviev V, "Time-Resolved Measurements of Plasma-Induced Momentum in Air and Nitrogen Under Dielectric Barrier Discharge Actuation," *Physics of Plasmas,* **17**, no. 113505, 2010.

Moreau E, "Airflow Control by Non-thermal Plasma Actuators," *Journal of Physics D: Applied Physics,* vol. 40, pp. 605-636, 2007.

[5] Macheret S, Shneider M and Miles R, "Magnetohydrodynamic and Electrohydrodynamic Control of Hypersonic Flows of Weakly Ionized Plasmas," *AIAA Journal,* **42**, no. 11, pp. 1378-1387, 2004.

Meyer R, Palm P, Ploenjes E, Rich J W and Adamovich I V, "The Effect of a Nonequilibrium RF Discharge Plasma on a Conical Shock Wave in a M=2.5 Flow," *AIAA Journal,* **41**, no. 5, pp. 465-469, 2003.

Minucci M, Toro P, Oliveira A, Ramos A, Chanes J, Pereira A, Nagamatsu H and Myrabo L N, "Laser-Supported Directed Energy "Air Spike" in Hypersonic Flow," *Journal of Spacecraft and Rockets,* **42**, no. 1, pp. 51-57, 2005.

Leonov S, Yarantsev D, Kuryachii A and Yuriev A, "Study of Friction and Separation Control by Surface Plasma," in *42nd AIAA Aerospace Sciences Meeting and Exhibit, AIAA-512*, Reno, Nevada, 2004.

Adelgren R, Elliot G, Crawford J, Carter C, Donbar J and Grosjean D, "Axisymmetric Jet Shear-Layer Excitation Induced by Laser Energy and Electric Arc Discharges," *AIAA Journal,* **43**, no. 4, pp. 776-791, 2005.

Samimy M, Adamovich I, Webb B, Kastner J, Hileman J, Keshav S and Palm P., "Development and Characterization of Plasma Actuators for High Speed Jet Control," *Experiments in Fluids,* **37**, no. 4, pp. 577-588, 2004.

Falempin F, Firsov A, Yarantsev D, Goldfeld M, Timofeev K and Leonov S, "Plasma control of shock wave configuration in off-design mode of M = 2 inlet," *Experiments in Fluids,* **56**, no. 54, 2015.

[6] Smith A, Gordeyev S, Ahmed H, Wittich III D and Paul M, "Shack-Hartmann Wavefront Measurements of Supersonic Turbulent Boundary Layers in the TGF," AIAA Paper 2014-2493.

[7] Gordeyev S, Smith A, Cress J and Jumper E 2014 Experimental Studies of Aero-Optical Properties of Subsonic Turbulent Boundary Layers *Journal of Fluid Mechanics* **740** pp 214-253

[8] Mack L M 1975 Linear Stability Theory and the Problem of Supersonic Boundary- Layer Transition *AIAA Journal* **13** 3 pp 278-289

[9] Anderson J D 2000 Hypersonic and High Temperature Gas Dynamics *Viscous Flow: Basic Aspects, Boundary Layer Results, and Aerodynamic Heating* Ch 6 Reston VA

[10] Aleksandrov N L, Kidysheva S V, Nudnova M M and Starikovskii A Y 2010 Mechanism of Ultra-Fast Heating in a Non-Equilibrium Weakly Ionized Air Discharge Plasma in High Electric Fields *Journal of Physics D: Applied Physics* **43** 255201

Popov N A 2011 Fast Gas Heating in a Nitrogen-Oxygen Discharge Plasma: I. Kinetic mechanism *Journal of Physics D: Applied Physics* **44** 285201

Shkurenkov I and Adamovich I 2016 Energy Balance in Nanosecond Pulse Discharges in Nitrogen and Air *Plasma Sources Science and Technology* **25** 015021

[11] Nishihara M, Takashima K, Rich J and Adamovich I 2011 Mach 5 Bow Shock Control by a Nanosecond Pulse Surface Dielectric Barrier Discharge *Physics of Fluids* **23** 066101

[12] NIST Chemical Kinetics Database National Institute of Standards and Technology [Online] Available: http://kinetics.nist.gov/kinetics/

[13] Rusterholtz D L, Lacoste D A, Stancu G D, Pai D Z and Laux C O 2013 Ultrafast Heating and Oxygen Dissociation in Atmospheric Pressure Air by Nanosecond Repetitively Pulsed Discharges *Journal of Physics D: Applied Physics* **46** 464010

[14] Popov N A 2011 Kinetic Processes Initiated by a Nanosecond High-Current Discharge in Hot Air *Plasma Physics Reports* **37** pp 805-817

Popov N A 2001 Investigation of the Mechanism for Rapid Heating of Nitrogen and Air in Gas Discharges *Plasma Physics Reports* **27** 10 pp 886-896

[15] Mack L M 1984 Boundary Layer Linear Stability Theory *Special Course on Stability and Transition of Laminar Flow* AGARD Report 709 pp 1-81

Fedorov A, Ryzhov A and Soudakov V 2013 Effect of Local Volume Energy Supply on High-Speed Boundary Layer Stability *43rd AIAA Fluid Dynamics Conference* San Diego California

[16] Leonov S, Houpt A and Falempin F 2015 Control of Hypersonic BL Transition by Electrical Discharge (feasibility study) *20th AIAA International Space Planes and Hypersonic Systems and Technologies Conference* Glasgow Scotland

[17] Raizer Y P 1991 Gas Discharge Physics, Berlin: Springer

[18] Tyson R K 1997 Principles of Adaptive Optics, New York: Academic

[19] Sontag J and Gordeyev S 2015 Non-intrusive Velocity and Density Measurements in Subsonic Turbulent Boundary Layer *46th AIAA Plasmadynamics and Lasers Conference* Dallas Texas

[20] Nightingale A and Gordeyev S 2013 Shack-Hartmann Wavefront Sensor Image Analysis: A Comparison of Centroiding Methods and Image Processing Techniques *Journal of Optical Engineering* **52** 071413

[21] Wang M, Mani A and Gordeyev S 2012 Physics and Computation of Aero-Optics *Annual Review of Fluid Mechanics* **44** pp 299-321

[22] Novikov A, Egorov I and Fedorov A 2016 Direct Numerical Simulation of Wave Packets in Hypersonic Compression-Corner Flow *AIAA Journal* **54** 7 pp 2034-50

[23] Beresh S, Henfling J, Spillers R and Pruett B 2010 Measurement of Fluctuating Wall Pressures Beneath a Supersonic Turbulent Boundary Layer AIAA-2010-305 Orlando Florida

[24] Houpt A W, Gordeyev S, Juliano T J and Leonov S B 2016 Optical Measurement of Transient Plasma Impact on Corner Separation in M=4.5 Airflow AIAA-2016-2160

Acknowledgments
The current work is supported by the FlowPAC Institute at the University of Notre Dame. A portion of this work (design of the SCD plasma actuator [16]) was previously supported by MBDA-France (Mr. Francois Falempin supervision). The authors would like to thank Dr. Alexander Fedorov for useful discussion pertaining to the nature of the disturbances present in our test cases.